

# List-Mode Maximum-Likelihood Reconstruction Applied to Positron Emission Mammography (PEM) with Irregular Sampling

Ronald H. Huesman\*, *Senior Member, IEEE*, Gregory J. Klein, *Member, IEEE*, William W. Moses, *Senior Member, IEEE*, Jinyi Qi, *Member, IEEE*, Bryan W. Reutter, *Member, IEEE*, and Patrick R. G. Virador

**Abstract**—We present a preliminary study of list-mode likelihood reconstruction of images for a rectangular positron emission tomograph (PET) specifically designed to image the human breast. The prospective device consists of small arrays of scintillation crystals for which depth of interaction is estimated. Except in very rare instances, the number of annihilation events detected is expected to be far less than the number of distinguishable events. If one were to histogram the acquired data, most histogram bins would remain vacant. Therefore, it seems natural to investigate the efficacy of processing events one at a time rather than processing the data in histogram format. From a reconstruction perspective, the new tomograph presents a challenge in that the rectangular geometry leads to irregular radial and angular sampling, and the field of view extends completely to the detector faces. Simulations are presented that indicate that the proposed tomograph can detect 8-mm-diameter spherical tumors with a tumor-to-background tracer density ratio of 3 : 1 using realistic image acquisition parameters. Spherical tumors of 4-mm diameter are near the limit of detectability with the image acquisition parameters used. Expressions are presented to estimate the loss of image contrast due to Compton scattering.

**Index Terms**—Image reconstruction, list-mode likelihood, mammography, positron emission tomography.

## I. INTRODUCTION

WE present a preliminary study of list-mode likelihood reconstruction of images for a positron emission tomograph (PET) specifically designed to image the human breast. The prospective device consists of small arrays of scintillation crystals for which depth of interaction is estimated. Except in very rare instances, the number of annihilation events detected is expected to be far less than the number of distinguishable events. If one were to histogram the acquired data, most histogram bins would remain vacant. Therefore, it seems natural to investigate

Manuscript received August 30, 1999; revised February 2, 2000. This work was supported in part by the National Cancer Institute of the U.S. Department of Health and Human Services under Grant R01-CA67911, by the National Heart, Lung, and Blood Institute of the U.S. Department of Health and Human Services under Grant P01-HL25840, and by the Director, Office of Science, Office of Biological and Environmental Research, Medical Sciences Division of the U.S. Department of Energy under Contract DE-AC03-76SF00098. The Associate Editors responsible for coordinating the review of this paper and recommending its publication were F. J. Beekman and M. A. Viergever. *Asterisk indicates corresponding author.*

The authors are with the Center for Functional Imaging, Lawrence Berkeley National Laboratory, University of California, Berkeley, CA 94720 USA (e-mail: rhuesman@lbl.gov).

Publisher Item Identifier S 0278-0062(00)05307-6.

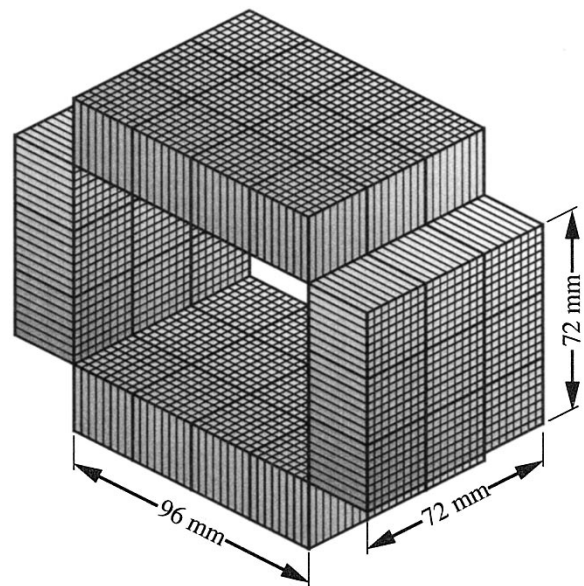


Fig. 1. Device Geometry. Four banks of detectors, each composed of  $8 \times 8$  arrays of crystals, define the geometry of the PEM camera. Each crystal is expected to distinguish depth of interaction to eight different levels. The tomograph has 172 million possible lines of response (LOR).

the efficacy of processing events one at a time, rather than processing the data in histogram format.

The methods we refer to as list-mode likelihood have been used for many years to analyze experiments in the field of high energy physics [1] and were suggested for PET image reconstruction in 1983 [2]. Renewed interest in list-mode likelihood PET image reconstruction is reflected by several recent publications [3]–[7].

A paradigm is presented that accurately accounts for detection probabilities in the absence of Compton scatter, either in the field of view or the detectors. It is able to compute the high resolution (unscattered) portion of the system matrix for a particularly irregular sampling geometry that includes depth of interaction information.

## II. GEOMETRY OF THE DEVICE

We give here an idealized model of the PET camera for which list-mode likelihood reconstruction is anticipated to be advantageous [8]. Individual crystals of scintillator (see Fig. 1) are

$3 \times 3 \times 30 \text{ mm}^3$  and modules consist of  $8 \times 8$  arrays of crystals. The tomograph consists of four banks of modules, two banks of  $3 \times 3$  modules left and right, and two banks of  $3 \times 4$  modules top and bottom. The imaging region is therefore  $72 \times 72 \times 96 \text{ mm}^3$ . Each bank is placed in coincidence with the other three, giving rise to 657 combinations of two modules placed in coincidence with one another. In addition to the 64 crystals in each module, the system will be able to distinguish the depth of interaction of the annihilation photon within a crystal to about one part in eight, so that 512 different signatures for a detection in a module are possible. Histogramming these data without loss of information will require  $657 \times 512^2 = 172$  million bins. Cubic voxel sizes of 3 mm or 2 mm will result in 18 432 or 62 208 voxels, respectively.

### III. LIKELIHOOD RECONSTRUCTION FOR LIST-MODE DATA

Although the likelihood function for list-mode data can easily be formulated from first principles [3], we give here a derivation that follows naturally from an expression for the likelihood function for statistically independent, Poisson-distributed histogram data. This is a natural progression in medical imaging in which data are ordinarily acquired in histogram format and statistical reconstruction techniques have been used to reconstruct statistically efficient medical images.

If the expected value for the  $k$ th bin is denoted by  $\nu_k$ , then the probability of observing  $n_k$  events in the  $k$ th histogram bin is given by the Poisson distribution  $P_{\nu_k}(n_k)$ , and the probability of observing the entire histogrammed dataset (of  $K$  bins) is given by the product

$$\prod_{k=1}^K P_{\nu_k}(n_k) = \prod_{k=1}^K \frac{e^{-\nu_k} \nu_k^{n_k}}{n_k!}.$$

The reconstruction problem is often posed as that of finding the distribution of radioisotope that would come “closest” to projecting the observed data. In maximum-likelihood reconstruction, “close” means likely or having high probability. The expected data can be written as

$$\nu_k = \sum_{j=1}^M F_{kj} \rho_j = (F\rho)_k$$

where  $\rho_j$  is the amplitude of the  $j$ th basis function used to model the radioisotope density, and  $M$  is the number of basis functions.  $F$  links a representation of the distribution of radioisotope with the expected number of histogrammed events in each bin. It is called the “system matrix” or the projection matrix and contains all of the physics of the data acquisition process. If the basis functions are normalized such that  $\rho_j$  is equal to the expected number of radioactive disintegrations from the  $j$ th basis function, then  $F_{kj}$  is the probability that a random event from the  $j$ th basis function is detected in the  $k$ th bin. We use cubic voxel basis functions to model the radioisotope distribution.

We can now express the probability of the observed histogrammed data as a function of the distribution of radioisotope

$$\begin{aligned} L(n_1, n_2, \dots, n_K | \rho_1, \rho_2, \dots, \rho_M) \\ = \prod_{k=1}^K \frac{1}{n_k!} e^{-(F\rho)_k} (F\rho)_k^{n_k}. \end{aligned}$$

This expression is also called the likelihood function with respect to our parameterization of the distribution of radioisotope. The natural logarithm is usually easier to work with, and therefore we write

$$\mathcal{L}(\rho) = \sum_{k=1}^K [n_k \ln(F\rho)_k - (F\rho)_k]$$

where the dependence on the parameters is explicit, and the constant term,  $\ln(n_k!)$ , has been dropped since it will not enter into the maximization of  $\mathcal{L}$  with respect to  $\{\rho_1, \rho_2, \dots, \rho_M\}$ .

For list-mode maximum-likelihood, we convert the first term to a sum over events instead of histogram bins. We also reverse the order of summation in the second term. If the bin number for the  $i$ th event is denoted by  $k_i$ , we have

$$\begin{aligned} \mathcal{L}(\rho) &= \sum_{i=1}^N \ln(F\rho)_{k_i} - \sum_{j=1}^M \varepsilon_j \rho_j \\ N &= \sum_{k=1}^K n_k, \quad \varepsilon_j = \sum_{k=1}^K F_{kj} \end{aligned}$$

where  $N$  is the total number of detected events, and  $\varepsilon_j$  is the efficiency of detecting events from the  $j$ th voxel.

A well-known, but slowly converging, method to maximize  $\mathcal{L}(\rho)$  is the expectation maximization (EM) algorithm [9]. For list-mode data the EM algorithm uses the following iterative stepping to obtain a solution:

$$\hat{\rho}_j^{n+1} = \frac{\hat{\rho}_j^n}{\varepsilon_j} \sum_{i=1}^N \frac{F_{k_i j}}{(F\hat{\rho}^n)_{k_i}}.$$

### IV. REGULARIZATION

In order to regularize the EM reconstruction we have used a technique described by Levitan and Herman [10]. The idea is to penalize the likelihood function with our prior knowledge of the nature of the image by using a Gaussian prior whose logarithm is of the form

$$-\frac{\gamma}{2}(\rho - \rho^*)^T H(\rho - \rho^*)$$

so that  $\rho$  can be coaxed to be close to  $\rho^*$  with some weighting given by  $H$ . The scalar  $\gamma$  is an overall strength parameter for the regularization. This is the appropriate penalty function for a Gaussian prior  $\rho^*$  with  $H$  equal to the inverse of the covariance matrix of  $\rho^*$ , and  $\gamma = 1$ .

If the matrix  $H$  is diagonal, the EM iterative process can easily be carried out since the set of equations to be solved in the M-step is not coupled. After substituting the identity matrix for  $H$ , the new stepping procedure is given by

$$\begin{aligned} \hat{\rho}_j^{n+1} &= \frac{1}{2} \left( \rho_j^* - \frac{\varepsilon_j}{\gamma} \right) \\ &+ \sqrt{\frac{1}{4} \left( \rho_j^* - \frac{\varepsilon_j}{\gamma} \right)^2 + \frac{\hat{\rho}_j^n}{\gamma} \sum_{i=1}^N \frac{F_{k_i j}}{(F\hat{\rho}^n)_{k_i}}}. \end{aligned}$$

This procedure may be appropriate for imaging distributions that are expected to be uniform or when a prior estimate of the distribution is obtained by a simpler approach such as filtered backprojection.

## V. THE SYSTEM MATRIX

To model the physics of the data acquisition process, we start with a simple model of two small, infinitely dense “black” detectors placed in coincidence and separated by a distance  $r$ . If the distance between the detectors is large compared to their size, then the solid angle of the second detector seen from the first is given by

$$\Omega_1 = \frac{\Delta a_2}{r^2}$$

where  $\Delta a_2$  is the area of the second detector projected on a plane perpendicular to the line between them. Therefore, the probability of detecting events from a point source placed between the detectors and very close to the first one is given by  $\Omega_1$  divided by  $2\pi$ , the solid angle of the half sphere. To get the expected number of coincident events observed from a unit intensity uniform planar source we multiply by  $\Delta a_1$ , the projected area of the first detector

$$\frac{\Delta a_1 \Omega_1}{2\pi} = \frac{\Delta a_1 \Delta a_2}{2\pi r^2}.$$

To a very good approximation, the coincident event rate from a uniform planar source placed between the detectors perpendicular to the line joining them is independent of the location of the source along this line. Therefore, the expected number of events observed by the two detectors is given by

$$\begin{aligned} \# \text{ events (black)} \\ = e^{-\int \mu_o(\ell) d\ell} \frac{\Delta a_1 \Delta a_2}{2\pi r^2} \int \rho(\ell) d\ell \end{aligned}$$

where the expression  $\int \rho(\ell) d\ell$  denotes the line integral of the source density between the two detectors,  $\int \mu_o(\ell) d\ell$  denotes the line integral of the linear attenuation coefficient between the two detectors to account for self-attenuation, and we have assumed that the source density  $\rho$  and the attenuation coefficient  $\mu_o$  vary slowly transverse to the line between the detectors.

Now taking account of the fact that the detectors are not in fact “black,” but have linear attenuation coefficient  $\mu$  and, therefore, a probability  $e^{-\mu w}$  of penetrating to the depth  $w$  before interacting, the probability of an annihilation photon being detected in the thickness  $\Delta w$  at the depth  $w$  is given by

$$e^{-\mu(w-\Delta w/2)} - e^{-\mu(w+\Delta w/2)} \approx \mu \Delta w e^{-\mu w}$$

where the approximation is valid for small values of  $\mu \Delta w$ , i.e., thin detectors. Now the expected number of events observed by two small detector volumes placed in coincidence and each embedded at some depth within a larger amount of detector material can be calculated using the formula

$$\begin{aligned} \# \text{ events} &= \mu^2 \Delta w_1 \Delta w_2 e^{-\mu w_1} e^{-\mu w_2} \\ &\times e^{-\int \mu_o(\ell) d\ell} \frac{\Delta a_1 \Delta a_2}{2\pi r^2} \int \rho(\ell) d\ell \\ &= e^{-\mu(w_1+w_2)} e^{-\int \mu_o(\ell) d\ell} \\ &\times \frac{\mu^2 \Delta v_1 \Delta v_2}{2\pi r^2} \int \rho(\ell) d\ell \end{aligned}$$

where  $w_1$  and  $w_2$  are the interaction depths in the two detector volumes  $\Delta v_1$  and  $\Delta v_2$ , respectively (with  $\Delta v_i = \Delta a_i \Delta w_i$ ). Neglecting many confounding physical effects of positron tomography (scatter, photon acollinearity, positron range, etc.), this equation is exact for infinitesimal volumes  $\Delta v_1$  and  $\Delta v_2$ .

We now put this into the context of the model of radioisotope distribution using normalized cubic voxels of volume  $V$ . The density integral is then given by

$$\int \rho(\ell) d\ell = \sum_{j=1}^M \ell_{kj} \frac{\rho_j}{V}$$

where  $\ell_{kj}$  is the length, within the  $j$ th voxel, of the line of response corresponding to the  $k$ th bin. Then we have

$$\nu_k = e^{-\mu(w_1+w_2)} e^{-\int \mu_o(\ell) d\ell} \frac{\mu^2 v^2}{2\pi r_k^2 V} \sum_{j=1}^M \ell_{kj} \rho_j$$

and

$$F_{kj} = \frac{\mu^2 v^2}{2\pi V} \left( \frac{\ell_{kj} e^{-\mu(w_1+w_2)} e^{-\int \mu_o(\ell) d\ell}}{r_k^2} \right).$$

Implementation of this form of the density integral gives an approximation of the probability which is only true for two infinitesimal detector volumes each of volume  $v$ . The correct implementation of this approach takes the average value of the term in the large brackets for all combinations of infinitesimal volumes of each of the two finite detectors taking part in the coincident detection. In addition, we now model self-attenuation within the imaging volume as a continuous uniform medium of attenuation coefficient  $\mu_o$ , so that

$$F_{kj} = \frac{\mu^2 v^2}{2\pi V} \left\langle \frac{\ell_{kj} e^{-\mu(w_1+w_2)} e^{-\mu_o(r_k-w_1-w_2)}}{r_k^2} \right\rangle$$

where  $\langle \cdot \rangle$  denotes the average value alluded to above. This model for self-attenuation assumes that the attenuating medium completely fills the field of view. This is the worst-case scenario, which can easily be relaxed, and a convex boundary for the attenuating medium can be determined from the emission data when the assumption is not satisfied.

Our implementation uses an approach that equally subdivides each relatively large detector into a set of smaller volumes, thus better approximating the infinitesimal detector volumes assumed in the discrete approximation. A detector is divided equally along each dimension so that a division level of  $D$  results in a set of  $D^3$  equal subvolumes. Connecting each subvolume between two detectors therefore results in  $D^6$  line integrals for each detector pair. This approach is intended to model the response function of the physical system of detectors described in Section II under the simplifying assumptions of a uniform attenuator in the field of view and the absence of confounding physical effects, especially Compton scatter.

## VI. EXPECTED COUNT RATES AND DATA SET SIZES

In order to estimate background rates for this analysis, we assume a subject weighing 70 kg and an injection of 1 mCi (37 MBq) of [F-18]-labeled deoxyglucose (FDG), which is uniformly distributed within the body. This activity density within our  $72 \times 72 \times 96$ -mm<sup>3</sup> field of view and an imaging time of 60 s gives about 16 million disintegrations within the imaging volume. The combined geometric and physical detection efficiency of the model outlined above is 14.5%, including self-attenuation, and results in about 2.3 million detected coincident events. (Histogrammed data would require 172 million bins.)

We have investigated density integral models with a single line integral between the depth decoded portions of the scintillator crystals and models that average many line integrals taken between more finely divided subvolumes of the depth decoded portions of the scintillator crystals. On-the-fly calculation of  $F_{kj}$  results in 10  $\mu$ s per event per iteration of the EM algorithm for each line integral in the model (23 s per iteration for 2.3 million events). If the nonzero factors  $F_{kj}$  are stored on disk, an average of 350 bytes are required for each event, and iteration speed is 20  $\mu$ s per event for single line integrals. These numbers are dominated by disk speed and increase to 1000 bytes per event and 40  $\mu$ s per event, respectively, for integral models which average many lines. Results are averages of 2-mm and 3-mm voxel tests, and timing was done on an SGI Octane 225 MHz MIPS R10000. For 2-mm voxels, the 64 line integral model appears necessary to avoid artifacts in the calculated efficiency map.

## VII. SIMULATIONS

Simulation results focus on the tomograph's ability to detect small tumors in data obtained from a typical breast examination. For simulations of acquired data, a linear attenuation coefficient of 0.01  $\text{mm}^{-1}$  was used for self-attenuation, and a linear attenuation coefficient of 0.1  $\text{mm}^{-1}$  was used for crystal penetration. The effects of photon Compton scatter were not modeled. Photons that interact in any way in the field of view are assumed undetected, and photons that interact in the detectors are assumed to do so once in a single well-defined depth decoded portion of a scintillator crystal. (We discuss the effects of Compton scatter in the next section.) Results show that despite the irregular sampling for this tomograph and a field of view that extends to the detector faces, high resolution, isotropic reconstructions may be obtained throughout the entire imaging volume.

Fig. 2 shows the expected efficiency of the device using 3-mm voxels. As shown in Fig. 2(a), the expected efficiency ranges from about 0.15 to 0.40 in the central plane and decreases to about 0.01 in the outer planes. Calculations of the efficiency using the analytically defined system matrix and 1, 64, and 729 line integrals per detector line of response (LOR) are seen in Fig. 2(b)–(d), respectively. In these images, the results are shown as the difference image between the Monte Carlo estimation and the analytically calculated results. Comparison of these results show that for the 3-mm voxel case, the center voxel efficiencies are accurate using any of the models, but accurate estimation of corner voxel efficiencies requires a model using more line integrals. This effect is seen more dramatically for the case of 2-mm voxels. As seen in Fig. 3, comparison of the Monte Carlo images with the difference images of Fig. 3(b)–(d) show that artifacts are present throughout the volume if a multiple line integral model is not used.

Reconstructions of a flood phantom with 16 million total disintegrations within the imaging field of view are presented in Fig. 4. The images represent the reconstruction of approximately 2.3 million detected events. For all reconstructions, the penalty function of the Gaussian prior was set such that  $\gamma/\rho^* = 0.1$ , and the EM algorithm was run until the penalized likelihood function reached a maximum. The coefficient of the uniform

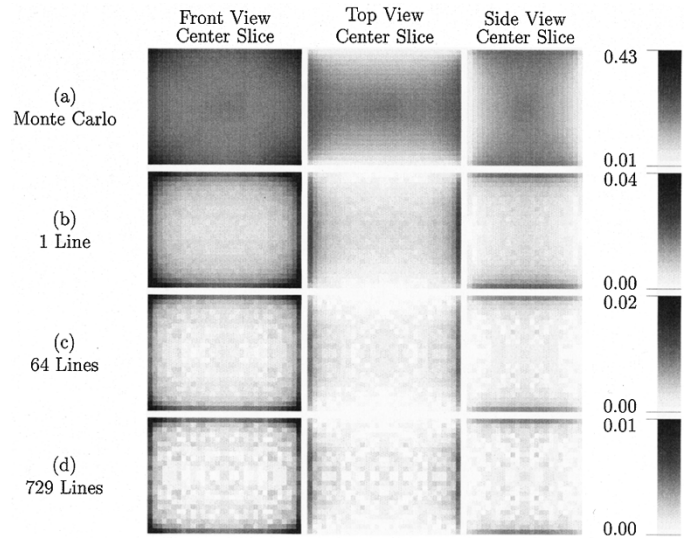


Fig. 2. PEM Efficiency (3-mm voxels). Detection efficiency obtained via Monte Carlo is presented in (a). Absolute difference images between the Monte Carlo result and analytically calculated efficiency using 1, 64, and 729 line integrals for each LOR are shown in (b), (c), and (d), respectively. Comparison of these images and the relative scale of the errors reveals that the simpler models produce errors principally at the corners.

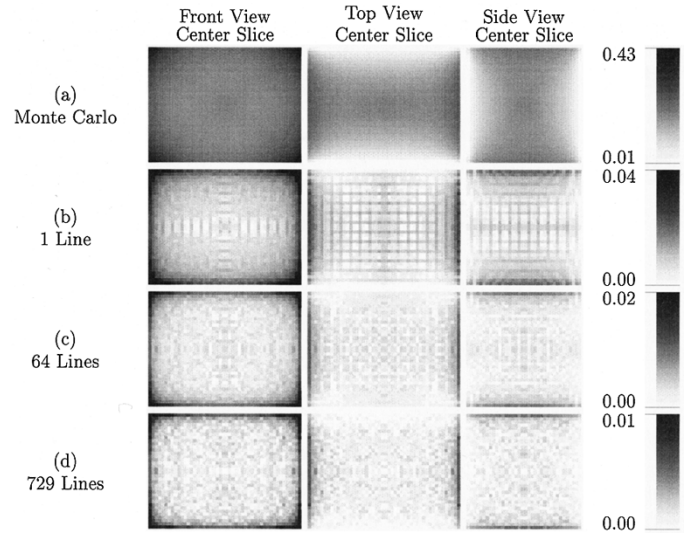


Fig. 3. PEM Efficiency (2-mm voxels). Detection efficiency obtained via Monte Carlo is presented in (a). Absolute difference images between the Monte Carlo result and the analytically calculated efficiency using 1, 64, and 729 line integrals for each LOR are shown in (b), (c), and (d), respectively. For the 2-mm voxel case, rather severe artifacts are present using the single line integral method (b). It appears that at least a 64 line integral technique is required to prevent large errors.

prior  $\rho^*$  was set to the total number of detected events divided by the number of voxels and corrected upward to reflect the average efficiency of 14.5% within the field of view. Results using the 729 line integral model are seen in Fig. 4(a), and for comparison, the reconstructions, using the 64 and 1 line integral models, are shown in Fig. 4(b) and (c). As was seen in the calculated efficiency volumes of Figs. 2 and 3, the model using more line integrals per LOR produces images with fewer artifacts, especially at the corners of the imaging volume. The reconstructions are reasonably uniform and have similar qualitative noise characteristics. Particularly encouraging is the fact that for 2-mm voxels,

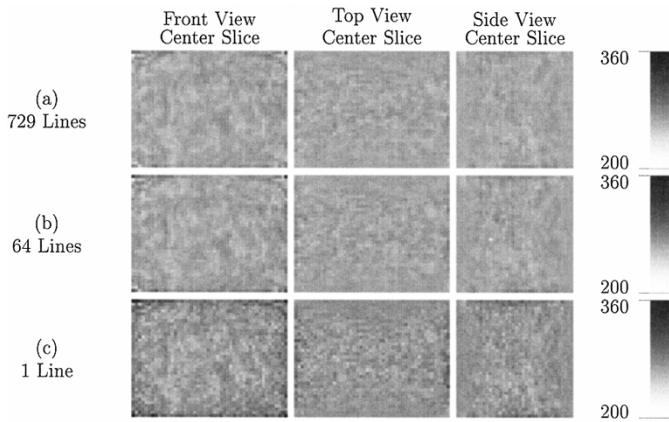


Fig. 4. Flood Phantom Reconstruction. Flood phantom reconstruction using 2-mm voxels and 729, 64, and 1 line integrals for each LOR are shown in (a), (b), and (c), respectively. Reasonably flat reconstructions are obtained in all cases, though considerably more noise and errors in the corner voxels are present in case (c).

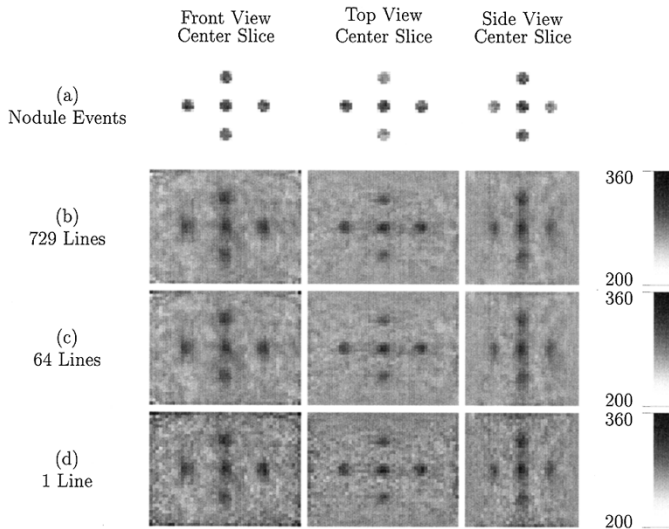


Fig. 5. Nodule Simulation (8-mm spheres). Seven 8-mm spherical nodules simulating breast tumors are seen against a noiseless background in a 2-mm voxel volume in (a). Voxel intensities are proportional to the number of events generated and detected from the spheres. Reconstructions using a simulated tumor-to-background tracer density ratio of 3:1 reveal that the nodules are easily detectable using either the 729, 64, or 1 line integral/LOR models, seen in (b), (c), or (d), respectively.

reconstruction artifacts do not appear when using a voxel size less than the size of the detectors.

To test the ability of the tomograph and reconstruction algorithm to detect well-defined tumors in a typical breast examination, a mathematical phantom of seven 8-mm diameter spheres was created. The phantom on a noiseless background is seen in Fig. 5(a). List-mode events from the spherical phantom were added to the flood phantom background such that the radio-tracer density ratio between the nodules and the background was 3:1. This dataset was then reconstructed using the same EM algorithm as described previously. Comparison of the images produced using 729, 64, and 1 line integral model, shown in Fig. 5(b)–(d), respectively, reveal that simulated tumors of this size and contrast are easily detected using any of the models.

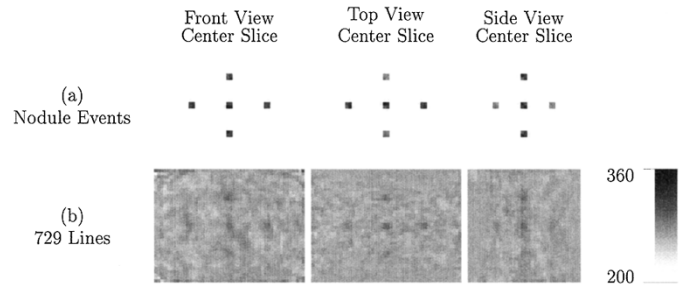


Fig. 6. Nodule Simulation (4-mm spheres). Seven 4-mm spherical nodules against a noiseless background are seen in (a). Voxel intensities are proportional to the number of events generated and detected from the spheres. Reconstruction (2-mm voxels and 729 line integrals) of the phantom with a target-to-background tracer density ratio of 3:1 shows that even the 4-mm spheres are detectable when scatter is not included in the simulation (b).

Here, the 729 and 64 line integral models appear to perform equally.

Results of a more challenging simulation are presented in Fig. 6. Here, the diameter of the spherical nodules was decreased from 8 mm to 4 mm. Reconstructed results show that even in this case, for which the number of events arising from the spheres is reduced by a factor of eight, the nodules are usually detectable under the idealized assumptions we have made concerning scatter backgrounds. Note that even though the two spheres in the outer planes may be difficult to see in this case, the simulated imaging parameters here are quite conservative, and either an increase in patient dose or imaging time will improve contrast-to-noise ratios.

## VIII. COMPTON SCATTER

An important physical effect that we have neglected in this investigation is the detection of photons that have Compton scattered. In our model of self-attenuation, we have assumed that photons that interact in any way in the field of view remain undetected. Actually, many of these scattered photons escape the imaging volume and are well above the energy threshold of the detectors. Similarly, we have assumed that any photon that interacts in the detectors does so in a single well-defined depth decoded portion of a scintillator crystal, which we can unambiguously determine. Some of these photons also Compton scatter, giving rise to ambiguities which preclude determination of the first interaction point, or they can deposit energy below the detector threshold and are undetected. These effects weaken our analysis, but there are some general statements that can be made about the consequences of scatter in this application.

We consider three types of Compton scattering that affect the conclusions of this paper: photons scatter in the field of view and are detected, photons scatter in the detectors and preclude precise determination of a single interaction point, and photons scatter in the detectors but are undetected. For the physiological conditions assumed in this investigation (isolated lesions in a uniform background of activity), we have performed a Monte Carlo calculation of the average background due to these types of scatter. This calculation uses the appropriate energy-dependent cross sections for the interaction of photons in water (in the field of view) and in lutetium oxyorthosilicate (commonly

referred to as LSO, the scintillator used in our device). (Using these linear attenuation coefficients, the average efficiency for the simplified detection model is reduced to 13.8% instead of 14.5% as quoted above.) For an energy threshold of 270 keV, we have found that: the fraction of annihilations that have a photon scatter in the field of view and are detected (case 1) is 0.040, the fraction of annihilations for which photons have not scattered in the field of view but have a photon scatter in the detector and are detected in the wrong location (case 2) is 0.040, and the fraction of annihilations for which photons have not scattered in the field of view, have both photons interact in the detectors, but have a photon remain undetected (case 3) is 0.052.

Scatter within the field of view appears to arise from a broad spatial distribution, and for purposes of approximating backgrounds we assume that annihilations from isolated sources that belong to case 1 will simply be indistinguishable from the uniform background of our physiological model. Detected events that scatter within the detectors have a much more limited spatial distribution [11], but for the purposes of this exercise we assume the worst-case scenario: annihilations from isolated sources that belong to case 2 will also be indistinguishable from the uniform background of our physiological model. Therefore, the average detection fraction of 0.138 for isolated sources (simplified detection model) is reduced by 0.040 (case 2) and 0.052 (case 3) to give 0.046. For annihilations originating in the background, 0.138 is increased by 0.040 (case 1) and reduced by 0.052 (case 3) to give 0.126. (The loss of events from isolated sources that contribute to the background is small and has been neglected in the estimation of background events.)

From these considerations we see that the effective relative efficiency of background events to target events is about  $0.126/0.046 = 2.7$ , so that a target-to-background activity ratio of 3 : 1 is effectively reduced to  $(3 - 1)/2.7 + 1 : 1 = 1.7 : 1$ . The total number of events acquired will be reduced by 9% ( $0.126/0.138 = 0.91$ ). Therefore, the most significant effect of scatter for this application is an effective loss of contrast. It is expected that scatter in the field of view can be appropriately modeled in the system matrix. Accounting for inter-detector scatter in the system matrix will result in better contrast than we have pessimistically assumed here.

## IX. SUMMARY

We have outlined a problem in nuclear medicine that may be amenable to analysis using the method of list-mode maximum-likelihood reconstruction. A methodology has been discussed, that is expected to yield desirable imaging properties and well-understood quantitative measures.

A paradigm has been presented that accurately accounts for detection probabilities in the absence of Compton scatter either in the field of view or the detectors. It is able to compute the high resolution (unscattered) portion of the system matrix for a particularly irregular sampling geometry that includes depth of interaction information.

Simulations show that 8-mm diameter spherical nodules are easily detected for an extremely conservative scanning paradigm: very low patient dose (1 mCi injection of FDG), short imaging time (1 min), and realistic target-to-background radio-tracer density ratio (3 : 1). Spherical nodules 4 mm in diameter are visible but more difficult to detect in this imaging environment, but a factor of 20 increase in detected events can easily be achieved by doubling the very low patient dose and increasing the imaging time to 10 min. Reconstruction time for this case would grow approximately linearly with the size of the list-mode data file.

Approximations have been presented that describe an effective reduction in the target-to-background activity ratio due to the effects of Compton scatter.

## REFERENCES

- [1] F. T. Solmitz, "Analysis of experiments in particle physics," *Ann. Rev. Nucl. Sci.*, vol. 14, pp. 375–402, 1964.
- [2] D. L. Snyder and D. G. Politte, "Image reconstruction from list-mode data in an emission tomography system having time-of-flight measurements," *IEEE Trans. Nucl. Sci.*, vol. NS-20, pp. 1843–1848, 1983.
- [3] H. H. Barrett, T. White, and L. C. Parra, "List-mode likelihood," *J. Opt. Soc. Amer. A*, vol. 14, pp. 2914–2923, 1997.
- [4] L. Parra and H. H. Barrett, "List-mode likelihood: EM algorithm and image quality estimation demonstrated on 2-D PET," *IEEE Trans. Med. Imag.*, vol. 17, no. 2, pp. 228–235, 1998.
- [5] A. J. Reader, K. Erlandsson, M. A. Flower, and R. J. Ott, "Fast accurate iterative reconstruction for low-statistics positron volume imaging," *Phys. Med. Biol.*, vol. 43, pp. 835–846, 1998.
- [6] —, "Fast accurate iterative three-dimensional Bayesian reconstruction for low-statistics positron volume imaging," *IEEE Trans. Nucl. Sci.*, vol. 45, pp. 1090–1095, 1998.
- [7] T. E. Nichols, J. Qi, and R. M. Leahy, "Continuous time dynamic PET imaging using list mode data," in *Information Processing in Medical Imaging*, A. Kuba, M. Šámal, and A. Todd-Pokropek, Eds. New York: Springer-Verlag, 1999, vol. 1613, Lecture Notes in Computer Science, pp. 98–111.
- [8] P. R. G. Virador, W. W. Moses, and R. H. Huesman, "Reconstruction in PET cameras with irregular sampling and depth of interaction capability," *IEEE Trans. Nucl. Sci.*, vol. 45, no. 3, pp. 1225–1230, 1998.
- [9] A. P. Dempster, N. M. Laird, and D. B. Rubin, "Maximum likelihood from incomplete data via the EM algorithm," *J. R. Statist. Soc. B*, vol. 39, pp. 1–38, 1977.
- [10] E. Levitan and G. T. Herman, "A maximum a posteriori probability expectation maximization algorithm for image reconstruction in emission tomography," *IEEE Trans. Med. Imag.*, vol. MI-6, pp. 185–192, 1987.
- [11] K. A. Comanor, P. R. G. Virador, and W. W. Moses, "Algorithms to identify detector Compton scatter in PET modules," *IEEE Trans. Nucl. Sci.*, vol. 43, no. 4, pp. 2213–2218, 1996.